

# MEMS Spatial Light Modulator for Phase and Amplitude Modulation of Spectrally Dispersed Light

Jonathan Dunayevsky and Dan M. Marom, *Senior Member, IEEE*

**Abstract**—We present a new micro-electro-mechanical system (MEMS) spatial light modulator (SLM) with a two-dimensional array of tightly-spaced square micromirrors (or pixels) designed to sag (or piston motion). This diffractive MEMS modulator is to be used for independently applying amplitude attenuation and phase control to spectrally-dispersed light along one dimension. The spectral phase and amplitude modulator operate in conjunction with a dispersive optical setup, where spatially resolved frequency components are to be incident onto and independently modulated by the device. The MEMS design is based on two common actuators per array column, in order to set the two degrees of freedom of amplitude and phase for every spectral component. This MEMS SLM is thus optimal in actuator/electrode count, especially when compared to conventional SLM where each pixel is independently actuated. The MEMS sag range is compatible with near-IR wavelengths used in the fiber-optic communication band. [2013-0040]

**Index Terms**—Optical modulation, Microelectromechanical device, microelectromechanical systems,

## I. INTRODUCTION

MODERN wavelength division multiplexing communication networks utilize dynamic wavelength provisioning, which can be based on optical filters [1], [2], channel blockers [3], wavelength selective switches [4], [5], and wavelength selective optical cross-connects [6]. Micro-electro-mechanical system MEMS based technologies are behind many of these solutions. Here we present a MEMS micromirror-based spatial light modulator (SLM) intended for modulating spectral amplitude and phase of optical communication signals, which can have many practical filtering applications benefitting from the favorable attributes of MEMS micromirrors: high-speed operation and polarization insensitivity.

Most SLMs work in either phase or amplitude modes, not both. However, in frequency filtering application it is desirable

Manuscript received February 4, 2013; revised March 27, 2013; accepted March 30, 2013. Date of publication June 25, 2013; date of current version September 27, 2013. This work was supported in part by the Israel Science Foundation under Grant 1359/07, in part by Xtellus (now Oclaro Corporation), and in part by the Peter Brojde Center for Innovative Engineering. Subject Editor O. Solgaard.

J. Dunayevsky was with the Applied Physics Department, The Hebrew University of Jerusalem, Jerusalem 91904, Israel. He is now with Oclaro Corporation, Jerusalem 91450, Israel (e-mail: Jonathan.Dunayevsky@oclaro.com).

D. M. Marom is with the Applied Physics Department, The Hebrew University of Jerusalem, Jerusalem 91904, Israel (e-mail: danmarom@cc.huji.ac.il).

Color versions of one or more of the figures in this paper are available online at <http://ieeexplore.ieee.org>.

Digital Object Identifier 10.1109/JMEMS.2013.2262600

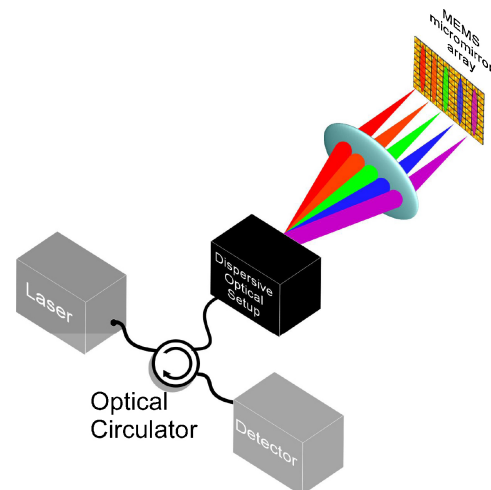


Fig. 1. Simplified diagram of typical setup for spectral filtering with a spatial light modulator placed in the spectrally dispersed plane.

to set both spectral amplitude and phase response across the signal bandwidth. Two modulators are often cascaded to achieve this capability [7], [8], but this solution imposes depth-of-field limitations leading to a reduction of resolution or additional imaging optics for a more complicated arrangement. MEMS mirrors that combine tip and piston motion have been shown to serve as phase and amplitude modulators, but the two actuators are typically coupled [9], [10].

Fig. 1 shows a generic optical frequency filtering arrangement that is used to project the dispersed light to the SLM and couple it back into the optical fiber. The configuration uses an optical circulator at the light input/output port, to separate the incoming signal from the modulated return light. The optical signal entering from the fiber passes through a dispersive element (diffraction grating, prism, or arrayed waveguide grating) and is projected on the SLM, such that each spectral component strikes at a different location on the SLM. The light is manipulated by the SLM and then reflected back, its spatial dispersion is undone, and coupled back into the optical fiber and out of the system via a circulator. The SLM can be implemented via liquid crystal [9]–[11] or MEMS technologies [12]–[16].

In this paper, we present a MEMS SLM based on a 2D array of piston motion micromirrors. This new MEMS SLM

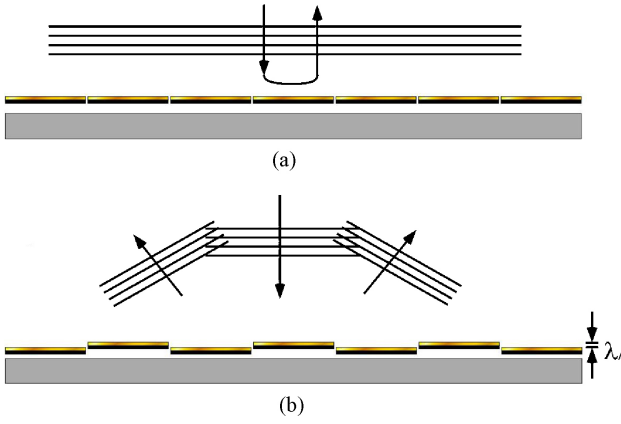


Fig. 2. Schematic diagram of single channel attenuation. (A) No sag, full reflection, and (B) sag of  $\lambda/4$ , diffraction into  $\pm 1$  orders, after [16].

is capable of fully modulating spectral components of incident light in both phase and amplitude. For this application there is no need to switch each micromirror independently, as is common in liquid crystal [17], [18]. Such independent pixel addressing is better reserved for application requiring a real 2D SLM [19]. Instead, all the odd/even mirrors of the same column can be switched together saving on actuator count and drive circuitry. It is the expressed goal of this device to independently modulate the amplitude and phase by controlling only two independent actuators/voltages per spectral component.

This paper is organized as follows: Section II, the theory of operation is presented, together with the design of the MEMS SLM. The fabrication process is described in Section III, and the characterization results are presented in Section IV. Finally, the conclusions of the paper appear in Section V.

## II. THEORY OF OPERATION

The basic principle for single wavelength component attenuation is based on an already proven technology of diffractive MEMS [22] (illustrated in Fig. 2). Conventional diffractive MEMS modulators are based on slender reflective strips, half of which are fixed and the other half movable, arranged alternately. The movable half can be set anywhere from fully in-phase to fully out-of-phase with the fixed half, achieving a controlled degree of interference upon reflection. With no voltage applied on the movable strips [Fig. 2(a)], the light is reflected back. With voltage applied on the movable strips [Fig. 2(b)], the actuated strips are pulled down a quarter wavelength, and creates a total path-length difference of  $\lambda/2$  between the light reflected from the movable strips and the fixed strips, thus interfering destructively and no light is reflected back in the incident direction. In this case the incident light is diffracted into higher-order diffraction orders, mostly the  $\pm 1$  diffraction orders. In this manner, the amplitude (or coupled energy) of the zero order term can be fully and continuously modulated.

Our new diffractive MEMS modulator enables independent motion of the even and odd mirror sets. Fig. 3 shows schematically the periodic phase delay associated with the

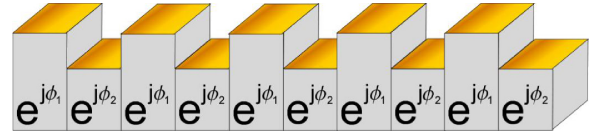


Fig. 3. Periodic phase modulation with adjustable values  $\phi_1$  and  $\phi_2$ , forming the basis of the amplitude and phase diffractive MEMS modulator.

interleaved reflective mirror modulator. One reflective mirror set is actuated to provide a  $\phi_1$  phase delay upon reflection, whereas the second set provides a  $\phi_2$  phase delay. For an incident plane wave, the modulator response,  $H[\phi_1, \phi_2]$ , is obtained by the zero'th diffraction order (i.e., reflection), where higher diffraction orders are not coupled back by the optical system, requiring a sufficiently large grating period (or small mirrors) to separate the diffraction orders. Hence the modulator response is simply the field average, or

$$H[\phi_1, \phi_2] = (e^{j\phi_1} + e^{j\phi_2})/2 \quad (1)$$

The magnitude and argument of the modulator response correspond to the amplitude and phase values that are imparted onto the reflected light. Greater insight into the operating principle of our diffractive MEMS modulator can be obtained after some manipulation of (1), obtaining

$$H[\phi_1, \phi_2] = \cos[(\phi_1 - \phi_2)/2] \cdot \exp[j(\phi_1 + \phi_2)/2] \quad (2)$$

Thus, we see that the phase average between the two reflective mirrors determines the reflected phase and the cosine of the phase difference between the two reflective mirrors determines the amplitude. Note that the representation of (2) cannot be directly related to the modulator's amplitude and phase as the cosine term can be negative for phase differences larger than  $\pi$ . In order for the modulator to modulate any phase within  $[0, 2\pi]$  and any amplitude within  $[0, 1]$ , simultaneously, each reflective mirror set should be capable of modulating continuous phase within  $[0, 2\pi]$ . That is for any desired amplitude and phase combination, there exists an actuator setting for the two phases that will satisfy the modulation target. To demonstrate this fact, let us assume that we wish to strongly attenuate the reflectivity and still control the phase. If we set  $\phi_2 = \phi_1 \pm \pi + \varepsilon$ , (the plus/minus sign is selected such that  $\phi_2 \in [0, 2\pi]$  and  $\varepsilon$  is a small phase detuning), then (2) simplifies to

$$H[\phi_1, \phi_1 \pm \pi + \varepsilon] = \mp \sin[\varepsilon/2] \cdot \exp\left[j\left(\phi_1 \pm \frac{\pi}{2} + \varepsilon\right)\right] \quad (3)$$

Thus the actuator's reflected response can achieve any attenuation setting by the phase detuning  $\varepsilon$ , and any absolute phase response (within  $0-2\pi$ ) can be obtained by judicious choice of  $\phi_1$  (operating point) and the phase detuning of  $\varepsilon$  (positive or negative small values).

Since the phase delay associated with the mirror displacement is twice the mirror travel, the mirror sag should be controlled within a range of 0–800 nm for optical communication wavelengths (around 1550 nm). Our new diffractive MEMS modulator utilizes densely packed, individually controlled columns of mirrors, as opposed to reflective strips of a conventional diffractive MEMS modulator. Additionally, the orientation of sampling is not in the spatial dispersion

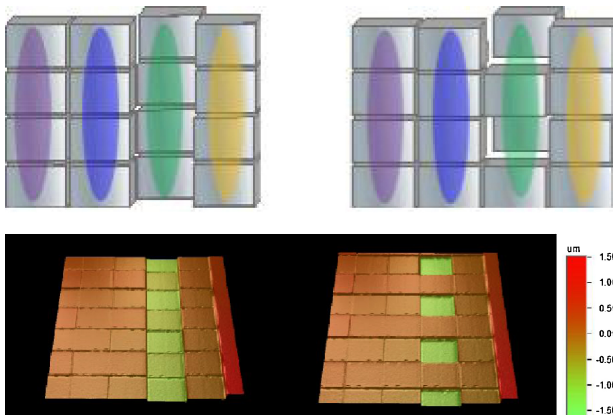


Fig. 4. Top: cartoon representation of single column activation with even and odd mirrors being actuated (left) and only odd mirrors actuated (right). Bottom: topography images of the same actuation patterns, collected by a WYKO interferometric microscope.

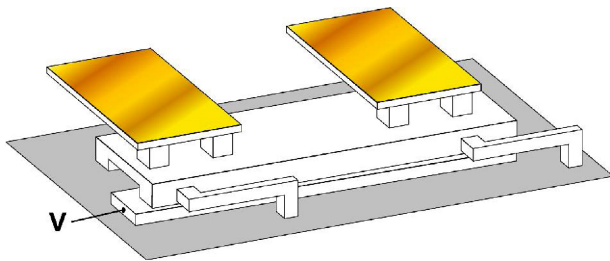


Fig. 5. Overall view of single MEMS actuator carrying one set of micromirrors (even or odd). A second actuator (not shown) carries the complementary mirrors. Jointly, both actuators (located under the mirrors) comprise a single column of the two dimensional SLM device.

direction, but orthogonal to it. The orientation change creates fixed width columns along the dispersion direction, where the complex amplitude of each column can be set by the even and odd mirrors of the column.

The basic SLM concept of operation is as follows: The modulator contains square pixels spanning a 2D rectilinear space (Fig. 4) with high fill factor; however, each column of the array is an independent module. All even and odd pixels of a column are attached to their own actuators which are hidden beneath the mirrors and actuated independently. All the even mirrors are attached to one beam and all the odd mirrors are attached to the other beam (Fig. 5). Each of these beams is part of an actuator that pulls in toward the substrate, pulling along the respective mirrors with it. Mutual displacement of the mirrors in the column [Fig. 4(left)] controls the phase upon reflection, while the relative displacement or sag of the mirrors [Fig. 4(right)] gives rise to constructive through destructive interference patterns, thus controlling the amplitude of each spectral component. With full spectral amplitude and phase control we can implement devices as filters, chromatic dispersion compensators, pulse shapers, and similar components.

### III. DESIGN

#### A. General Design

The MEMS design was subjected to two main constraints: activation voltage up to 100 V and design rules of the Sandia

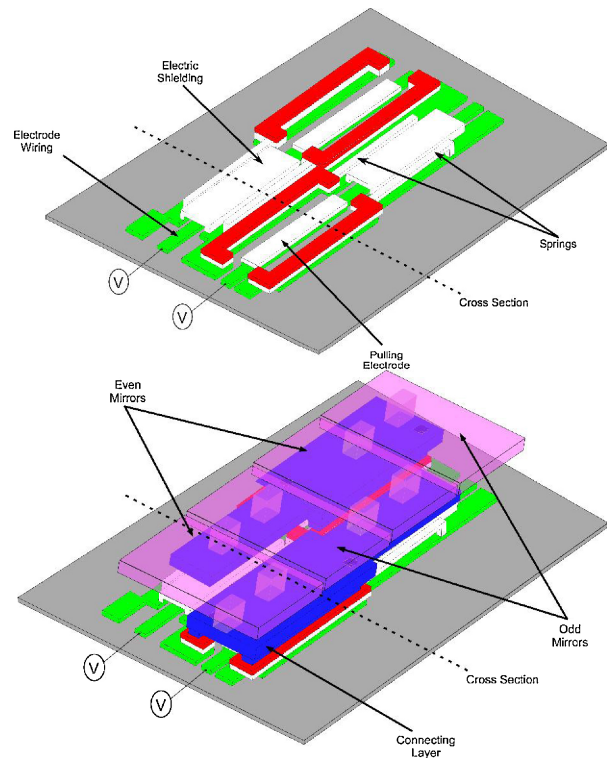


Fig. 6. Isometric view of single column actuator construction. Top: Diagram of lower part of the MEMS device (first three polysilicon layers). Bottom: Actuator beam and mirrors added on top (all 5 polysilicon layers shown).

SUMMiT V process [23]. In comparison to other multi-user solutions, such as those offered by MEMSCAP, the SUMMiT V process offers four movable MEMS layers and thin sacrificial oxide layers, which were instrumental for carrying out the under mirror mechanical actuator and motion range of our SLM design. Additionally we set a minimal mirror size objective for prescribing smooth modulation functions, as in staircase approximations to continuously varying functions. The mirror minimization is limited by process requirement such as  $1 \mu\text{m}$  minimum feature and misalignment tolerance between the layers.

The general design is presented in Fig. 6, which shows a segment of a single actuator column in isometric view. All even and odd mirrors/pixels (purple) of the column are attached to their own actuators which are hidden beneath the mirrors. Underneath each column are two beams (blue) onto which the mirrors attach. All the even mirrors are attached to one beam and all the odd mirrors are attached to the other. Each of these beams is part of the actuator that pulls in toward the substrate by electrostatic actuation, pulling along the mirrors attached to them. The beams are required to be stiff, such that there is minimal flexing and the mirrors remain on the same plane. On the other hand we wish to minimize the voltage that has to be applied to pull the beam down, so an edge supported solution is ruled out. Our solution is to support each beam by multiple slender spring legs distributed along the supporting beam (shown in white), much like a centipede, that attempt to spread the load and forces acting on the beam and ensure that pure piston motion is prescribed. These 'legs' are designed as flexure beams.

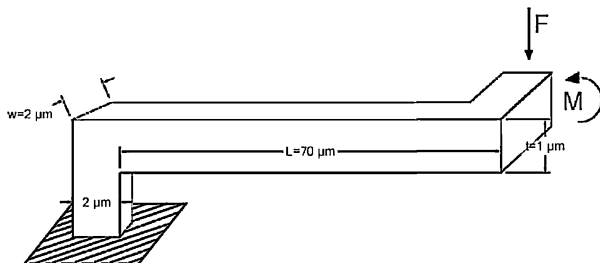


Fig. 7. Single support spring layout and force diagram.

Each spring (leg) is attached to the substrate at one end (fixed condition) and attached to the pistoning beam at the other end (no rotation condition) (Fig. 7). We can find the spring constant corresponding to the elastic interaction between the acting force,  $F$ , and the resulting end deflection,  $u$ , according to

$$K = \frac{F}{u} = \frac{12EI}{l^3} = \frac{Ewt^3}{l^3}, \quad (4)$$

where  $E$  is Young's modulus,  $l$  is the length of the beam, and  $I$  is the cross-sectional moment of inertia ( $I = w \cdot t^3/12$ ). Here  $w$  and  $t$  are the width and the thickness of the beam, respectively. The spring is implemented in a  $1 \mu\text{m}$  thick polysilicon layer (MMPOLY1). The width of the spring should be minimal. On one hand, the spring has to be as narrow as possible to meet the narrow column objective. On the other hand, the structure should be stiff to sideways movement. By setting the width of the spring to be twice the thickness, or  $2 \mu\text{m}$ , the stiffness in the sideways direction is four times greater than the stiffness in the up-down direction. The length of the spring is chosen in balance with the attraction force acting on the actuator at the actuation voltage. The effective pulling area is approximately  $400 \mu\text{m}^2$ , due to the electrode area underneath a region supported by two springs. These parameters are later fine-tuned by finite element analysis (FEA) simulations.

Since the initial gap  $d_0$  is determined by the process to be  $3.8 \mu\text{m}$  (defined by SuMMiT V layers: SACOX2 ( $0.3 \mu\text{m}$ ) + MMPOLY2 ( $1.5 \mu\text{m}$ ) + SACOX3 ( $2 \mu\text{m}$ ), discussed later in Section D) and the activation voltage requirement, the maximum stiffness is calculated to be  $K = 2.16 \text{ N/m}$  by using

$$V_{PI} = \sqrt{\frac{8Kd_0^3}{27\epsilon_0 A_{\text{eff}}}} = \sqrt{\frac{8Ewt^3 d_0^3}{27\epsilon_0 A_{\text{eff}} l^3}}, \quad (5)$$

where  $A_{\text{eff}}$  is the effective pulling area,  $V_{PI}$  is the pull-in voltage of parallel plate actuator, and  $d_0$  is the gap between the plates. Two springs supports reside on opposite beam sides, for stability considerations, which means that the maximum stiffness of each spring is  $1.08 \text{ N/m}$ . From (5) the minimum length of the spring is calculated to be about  $70 \mu\text{m}$ .

### B. Overcoming Pull-in

To overcome the snap-in phenomena, from instability between the electrostatic force and the restoration force in parallel plate actuation, we have designed a nonlinear spring that increases its stiffness dramatically before the system

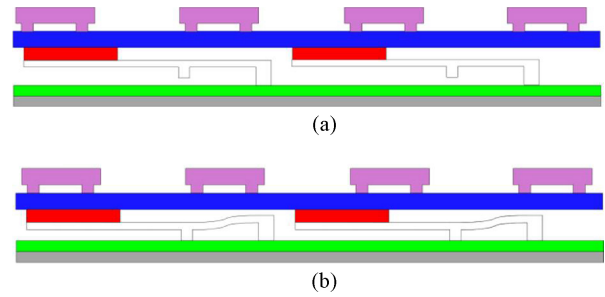


Fig. 8. Diagram demonstrating the stiction reduction mechanism. With no voltage applied (a), with voltage applied (b).

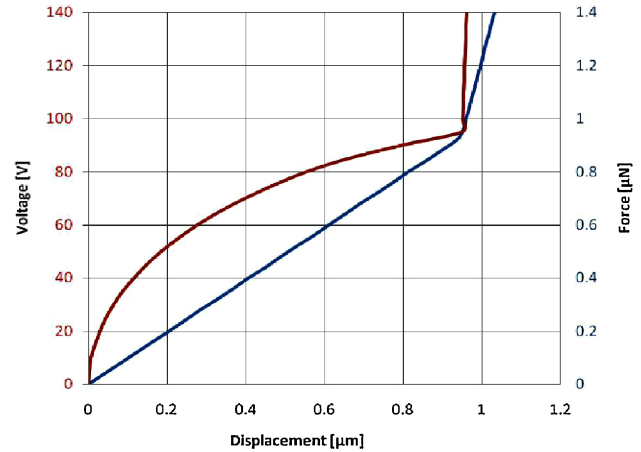


Fig. 9. (Blue) Simulated graph of applied force versus mechanical displacement, showing the change in spring stiffness the moment the dimple hits the substrate. (red) Simulated graph of applied voltage versus mechanical displacement. The simulation was done with COMSOL FEA software.

reaches the unstable state. A small protrusion on each spring bottom is placed, such that it will come into contact prior to snap-down (Fig. 8). Upon contact of the protrusion with the substrate, further beam bending occurs about the new contact point, resulting in reduced beam length and greatly enhanced stiffness. This nonlinear spring behavior raises the snap-down threshold significantly. The dimple is designed to be  $0.5 \mu\text{m}$  above the substrate. The dimple location is designed for allowing  $\sim 1 \mu\text{m}$  edge displacement before contact.

Fig. 9 shows the influence of the applied voltage on the sag of the mirror. These FEA results confirm that the snap-in occurs at voltages much higher than  $400 \text{ V}$  with the nonlinear spring, whereas without it snap-in would occur at  $130 \text{ V}$ .

### C. General Layout

The SLM is composed of a two dimensional micromirror array, consisting of 12 columns along the dispersion axis and 33 mirrors in the orthogonal direction (per column). The dimension of each micromirror is  $35 \mu\text{m} \times 35 \mu\text{m}$ , with  $1 \mu\text{m}$  gap between the mirrors (fill factor of 94.35%). The column count (spectral extent) can scale to support as many columns as desired, as there is no electrical routing issue since only two actuators/voltages are supplied per column, and the column height (and mirror count) can be increased further in our design, due to the distributed support solution. Fig. 10 shows a microscope image of the fabricated chip.

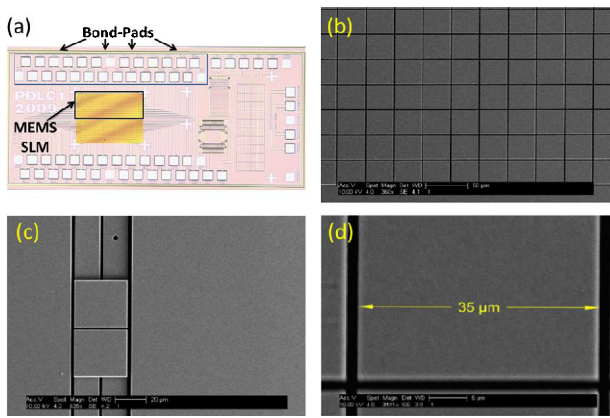


Fig. 10. Images of fabricated chip. (a) microscope image of entire chip (gold false colored here) and (b-d) scanning electron micrograph images of the device. (b) shows the two-dimensional SLM mirrors, (c) is a zoomed view of a single mirror of width  $35\ \mu\text{m}$ , and (d) a test actuator (not part of the SLM array), which shows the two actuators comprising a SLM column, with one mirror on each actuator.

*D. Fabrication*

The fabrication process utilized the multiuser process ‘Sandia Ultra-planar Multilayer MEMS Technology V’ (SUMMiT V) offered by Sandia National Laboratories. SUMMiT V is a five-level, surface micromachining technology featuring four mechanical layers of polysilicon above a thin, highly-doped polysilicon electrical interconnect and ground plane layers. Sacrificial oxide is sandwiched between each polysilicon level. The thin sacrificial films define the amount of mechanical motion in the vertical direction. Minimal lithography features and alignment accuracy are  $1\ \mu\text{m}$ . The layers of polysilicon are designated from the substrate up as MMPOLY0–MMPOLY4. Similarly, the sacrificial oxide layers are designated as SACOX1–SACOX4.

The device construction can be fully appreciated with the aid of Fig. 11, which shows a single column cross sectional view, layer by layer. Within the cross section two actuators are visible; the right actuator is cut through the actuation region (will be formed by a raised electrode acting upon the beam carrying a mirror). The left actuator is cut through the spring region and the conductor is shielded. The alternating actuation regions enable us to widen the actuator a bit, so that it acts predominantly as a parallel plate device.

We start off with  $0.3\ \mu\text{m}$  thick Poly0 layer (purple) composed of polysilicon deposited on a silicon wafer with  $0.6\ \mu\text{m}$  layer of thermal oxide and  $0.8\ \mu\text{m}$  silicon nitride deposited on it (gray) and patterned to define the electrode and ground plane regions [Fig. 11(a)]. The electrodes are  $60\ \mu\text{m} \times 6\ \mu\text{m}$  rectangles with rounded edges (to prevent unwanted electrical effects). The electrodes of the same actuator are wired together with  $3\ \mu\text{m}$  wide lines that are also defined at this stage. The grounded regions around the electrodes act as electric shields so that when voltage is applied on one electrode the other electrodes will not accumulate electric charge. Since the subsequent oxide layer is  $2\ \mu\text{m}$  thick, Poly0 cuts as wide as  $3.5\ \mu\text{m}$  will fill the cuts in the polysilicon layer and create a uniform layer of oxide above it (with small insignificant sags in the oxide layer).

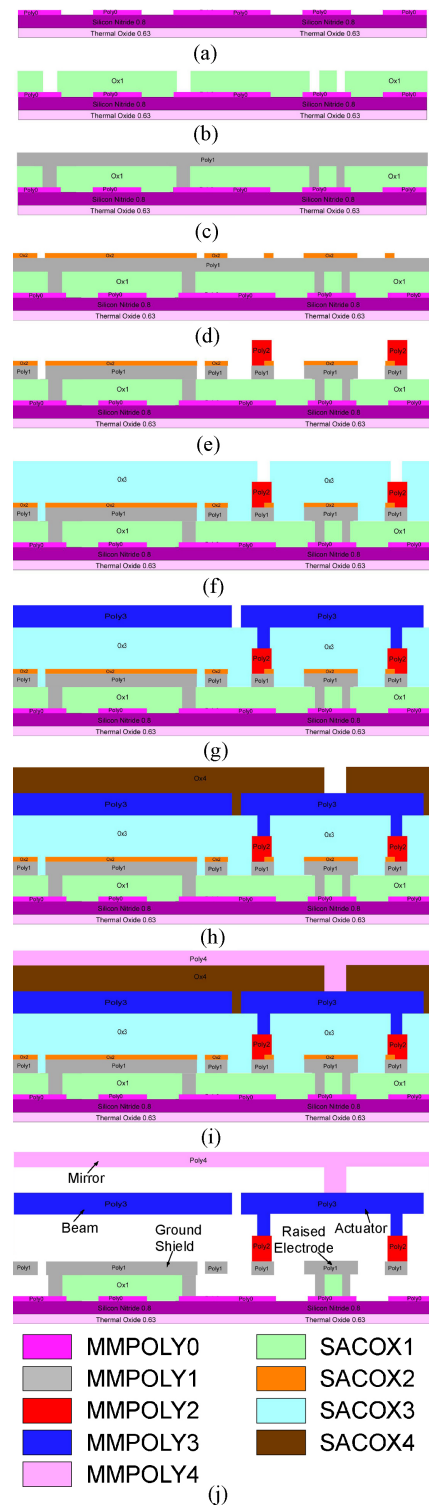


Fig. 11. Process flow description, following the SuMMiT V convention.

A  $2\ \mu\text{m}$  oxide layer is deposited and patterned [green, Fig. 11(b)] to raise the actuator above grounded shield, with cuts to the electrode and spring anchor points. We also create small cuts to create a shielded tunnel about the wiring of the electrodes. Those cuts are narrow enough ( $1\ \mu\text{m}$ ) so that the next MMPOLY1 layer will fill the cuts in the oxide and yet create as uniform as possible polysilicon layer MMPOLY1.

In the next stage  $1\ \mu\text{m} \times 1\ \mu\text{m}$  dimple cuts are made to create dimples in the middle of the spring (not shown in Fig. 11 since the cross-section is at a different location). This dimple will create the nonlinear spring that will significantly increase the pull-in voltage and prevent the structure from snapping down.

In the following stage  $1\ \mu\text{m}$  thick MMPOLY1 is deposited [gray, Fig. 11(c)]. This polysilicon layer is not patterned at this stage, but it will be cut along with the MMPOLY2 layer at a later stage in the process. This way no misalignment problems may accrue between these two layers

The next  $0.3\ \mu\text{m}$  thick SACOX2 layer is deposited [orange, Fig. 11(d)] and creates a hard mask for MMPOLY1. The regions in MMPOLY1 that are covered by this oxide or by MMPOLY2 will not be etched away. The regions that will be covered by MMPOLY2 but not by the SACOX2 will not be etched away but in those regions MMPOLY1 will be connected to the MMPOLY2 layer. We are interested to create the raised electrode (rectangles with rounded edges), spring ( $70\ \mu\text{m} \times 2\ \mu\text{m}$  beams connected at the end to a rectangular plate), and the wire tunnel (rectangular plate covering the wire) only in MMPOLY1. Some oxide was left on the sides to insure that the formation of the electrodes and the sides of the actuator is to be governed by SACOX2 mask. That should insure the inner sides of the actuator structures are equally distanced from the electrode.

In the next stage  $1.53\ \mu\text{m}$  thick MMPOLY2 [red, Fig. 11(e)] is deposited and patterned. As mentioned earlier, only the unprotected regions are etched away.

Now the electrodes, springs, and wire protecting covers/shields are complete.  $66\ \mu\text{m} \times 2.5\ \mu\text{m}$  beams created in MMPOLY2 are used to heighten the actuator and to create sufficient gap between the raised electrode and the actuator's bottom surface. This gap will enable the desired actuation.

The following stage thick SACOX3 [pale blue, Fig. 11(f)] is deposited, planarized to  $2\ \mu\text{m}$  thickness, and patterned. Thus, at the end of SACOX3 deposition we get a smooth oxide surface and all the topography created by previous layers is filled with oxide. After the planarization,  $62\ \mu\text{m} \times 1\ \mu\text{m}$  anchor cuts are made above the MMPOLY2 beams to connect between the following MMPOLY3 layer to the structure underneath.

The next stage is deposition and patterning of  $2.25\ \mu\text{m}$  MMPOLY3 [blue, Fig. 11(g)] forming long beams that are connected to MMPOLY2 only in the electrode regions. This layer completes the actuators by forming a box above the electrode.

The planarization of the SACOX3 layer insures that the bottom surface of the beam/actuator is smooth and parallel to the electrode surface which is critical for the actuator performance. Until this stage all the actuators in the column are actually separate units. The beams that are formed in MMPOLY3 are designed to connect all those separate units into one distributed actuator. This insures that all the mirrors connected to the column move together. Etch release holes are made in the structure to facilitate hydrogen-fluoride (HF) penetration into the structure, and etch away the exposed sacrificial oxide [etch hole visible in Fig. 10(d)]. Easy access of HF into the structure insures that the structure will be successfully released.

The last  $2\ \mu\text{m}$  thick oxide layer [SACOX4, brown, Fig. 11(h)] is deposited, planarized, and patterned. Similarly to SACOX3 the topography created by MMPOLY3 is filled with oxide and the upper surface of the layer is polished by CMP process. The polishing of the SACOX4 layer insures that the above layer will be flat which is critical as the last layer forms the mirrors.

Cuts are etched to anchor the mirrors to a lower polysilicon layer. These cuts are made as narrow as possible to insure the flatness of the mirrors that will be deposited above, yet the cuts have to be big enough to support the mirrors.

The last deposited layer is  $2.25\ \mu\text{m}$  thick MMPOLY4 [pink, Fig. 11(i)]. This layer is used to construct the mirrors. The mirrors are  $35\ \mu\text{m} \times 35\ \mu\text{m}$  squares with  $1\ \mu\text{m}$  gap between them.

After all the SACOX and MMPOLY layers are deposited and patterned, bond pads were conventionally aluminum metallized at the wafer level by Sandia. Wafers are then diced and individual MEMS die undergo HF release, etching away all the exposed sacrificial oxide, leaving only polysilicon behind. The released structure is shown in Fig. 11(j). The oxide surrounding the wires that is shielded by polysilicon is not etched. This electric shielding prevents the charged wires from applying attractive forces on the springs. No exposed oxide that can be subjected to charging remains.

Mirror metallization was performed at the Unit of NanoFabrication of the Hebrew University using a shadow mask on the release structure. We deposited  $5\ \text{nm}$  titanium as an adhesive layer and  $50\ \text{nm}$  of gold above it as a reflection layer using a VST TFDS 141E vacuum coater.

### E. Packaging

A UV adhesive was used to glue the MEMS chip (edge bead) onto a commercially available ceramic carrier. The MEMS chip was then wire-bonded to the ceramic carrier's bond pads.

## IV. CHARACTERIZATION RESULTS

### A. Sag Versus Voltage Behavior

An interferometric microscope was used to characterize the MEMS array and acquire topography information. It seems from the measurements [Fig. 4(bottom)] that the even and odd mirrors are slightly displaced from each other in elevation (about  $100\ \text{nm}$ ). This displacement originates from undesired curvature along each actuator (column direction), most likely from stress in the actuating beam (Fig. 12). We believe that the polysilicon layers comprising the actuator beam (MMPOLY1–3) have residual stress from the deposition process and are the source of this curvature. We further see that the even and odd mirrors of the same column are identically curved but offset in center position. This is due to the oppositely directed supporting springs (Fig. 6). Redesigning the supporting springs such that they are identically oriented for both actuators will remove this small offset. The effect of the offset in the current MEMS SLM can be minimized by calibrating the applied voltages and level the mirrors (requiring excess mirror travel range). We applied 0–130 Volts on a single actuator within

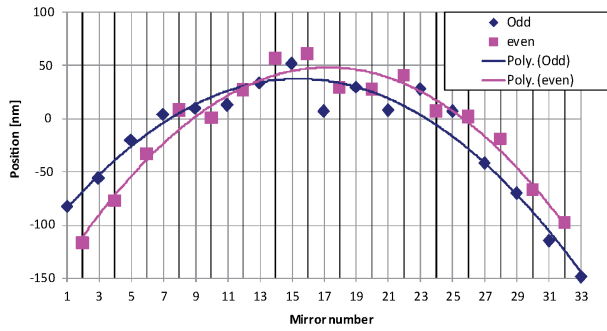


Fig. 12. Curvature over array measurement and estimation of actuator curvature.

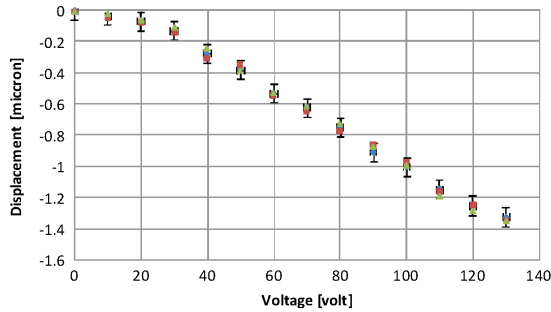


Fig. 13. Sag vs. voltage graph, data extracted from measurements by an interferometric microscope. The net displacement at each voltage for three mirrors of the same column shown (red, green and blue on the graph). The shown displacement of each mirror was averaged over the surface of that mirror; error bars denote displacement noise over mirrors.

the interferometric microscope, and charted the sag-voltage dependence (Fig. 13).

During this measurement we also measured the sag of the adjacent mirrors (electrical and/or mechanical crosstalk both to adjacent actuator and to neighboring columns). We did not observe any coupling between adjacent actuators within the resolution of the interferometric microscope.

The measurements show that the desired 800 nm displacement was obtained at 100 V, as predicted in the design phase. For 130 V, the mirrors sag by  $1.3 \mu\text{m}$  (more than  $3\pi$  phase delay). This excess range can be beneficial to balance out the two actuators of a column, as previously discussed. However, Fig. 13 does not exhibit the expected nonlinear spring behavior from simulations in Fig. 9. At low voltages the behavior is parabolic, as expected. However, instead of exhibiting a sharp inflection point, due to the dimple hitting the substrate, we see a nearly linear voltage-sag behavior above 60 V. We believe that this is a result of the actuator curvature, leading to the dimples not touching the substrate simultaneously. This makes the stiffness transition smoother. Furthermore, the beam curvature results in a varying displacement to the ground electrode along the beam, which affects the capacitance change per beam sag at every position. This effect modifies the force component operating on the beam, which may further lead to the extended linear sag behavior. Finally, our mirror sag modeling was based on a two-dimensional simulation (assuming the beam length is the third dimension). Since the electrodes are segmented in practice, a three-dimensional simulation may better account for

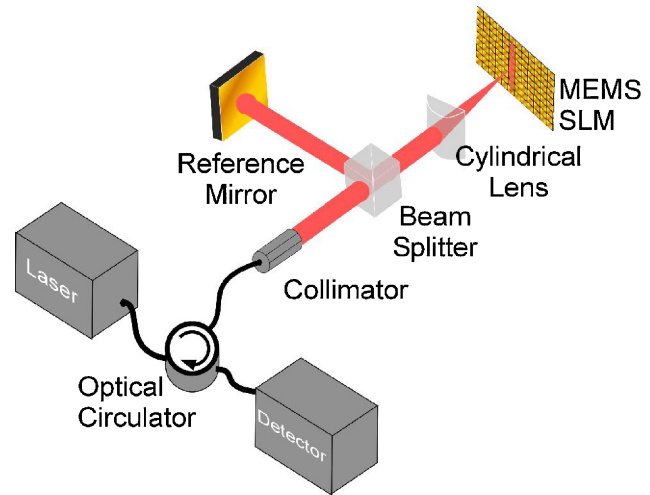


Fig. 14. The experimental setup for evaluating the full optical reflection characteristics. The reference mirror is blocked for the amplitude response, and the interference is recorded for the phase response.

the experimental observation, especially if the stress induced beam curvature is added.

From Fig. 13 it seems that the stiffness of the spring is a bit weaker than designed (compared to Fig. 9). We believe this is due to slight over-etch of the spring's width. Additional supporting evidence is found in the actuator's resonance frequency, discussed below (Section IV-D).

### B. Mirror Flatness

The single mirror ( $35 \mu\text{m}$  on a side) radius of curvature was measured by the interferometric microscope to determine the flatness of the mirror. A single mirror radius of curvature was measured to be over 2 m (after metalization). The overall mirror array curvature was also measured. Along the column (indicating beam and actuator flatness), the radius of curvature was 847 mm. This flatness value is more than sufficient for the spectral filtering application with a beam size of  $\sim 1 \text{ mm}$ .

### C. Anti-Stiction Behavior

The relatively stiff spring stiffness result in a large enough restoring force to overcome stiction forces that occur upon contact. Dimples in the middle of the spring not only ensure that the structure can only touch down on few discrete points (small contact area) but also dramatically increase the stiffness of the spring the moment the dimples do touch. We have applied more than 200 V on a single column (our driver limit). The structure restores its position the moment we remove the voltage, and no stiction was observed.

### D. Optical Measurements

The experimental setup presented in Fig. 14 was assembled to test the amplitude and phase response of a single column modulator. This setup is basically an interferometer. Light with wavelength of 1550 nm from a laser delivered by single mode fiber, passes through an optical circulator, is collimated and then split by a beam-splitter. One beam strikes a reference mirror and is reflected back, while the other beam is focused

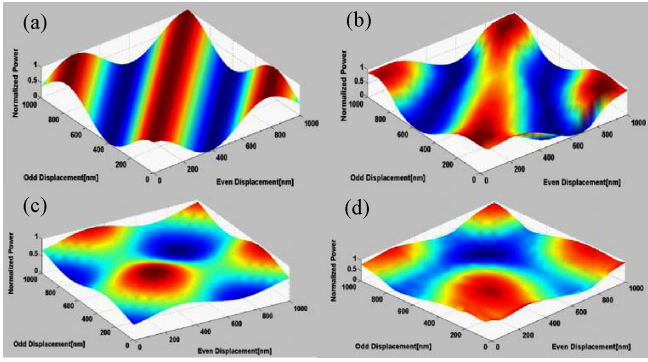


Fig. 15. Simulation and experimental setup results for registered normalized power when the reference arm is blocked, (a) and (b), respectively, indicating the amplitude of the light reflected from the SLM, and for registered normalized power when the reference arm is interfering with light reflected from the SLM, (c) and (d), respectively, indicating the phase response. Full extinction (-26 dB) and full  $2\pi$  phase modulation are clearly demonstrated.

with a cylindrical lens on one column of the MEMS SLM and the reflected, modulated field can be expressed as (after (2), with phase values converted to MEMS sag):

$$\cos \left[ 2\pi \left( \frac{\text{Sag}_{\text{even}} - \text{Sag}_{\text{odd}}}{\lambda} \right) \right] \cdot \exp \left[ j2\pi \left( \frac{\text{Sag}_{\text{even}} + \text{Sag}_{\text{odd}}}{\lambda} \right) \right] \quad (6)$$

Both beams are reflected back, combined in the beam splitter, and coupled back to the original input fiber through the circulator and to a power detector.

The registered optical power of the interference between the light that is reflected from the reference mirror and from the SLM is detected, providing information about the optical phase. The theoretical power [Fig. 15(c)] can be expressed as:

$$\text{Power} = \frac{1}{4} \cos^2 \left[ 2\pi \left( \frac{\text{Sag}_{\text{even}} - \text{Sag}_{\text{odd}}}{\lambda} \right) \right] + \frac{1}{4} + \frac{1}{2} \cos \left[ 2\pi \left( \frac{\text{Sag}_{\text{even}} - \text{Sag}_{\text{odd}}}{\lambda} \right) \right] \cos \left[ 2\pi \left( \frac{\text{Sag}_{\text{even}} + \text{Sag}_{\text{odd}}}{\lambda} \right) \right] \quad (7)$$

If we block the path to the reference mirror then no interference occurs and the power that is measured is the amplitude response of the modulated light. The theoretical power [Fig. 15(a)] can be expressed as:

$$\text{Power} = \cos^2 \left[ 2\pi \left( \frac{\text{Sag}_{\text{even}} - \text{Sag}_{\text{odd}}}{\lambda} \right) \right] \quad (8)$$

All combinations of voltages from 0 to 100 V (sufficient to piston MEMS micromirror sets by one wave, or  $2\pi$  retardation) were applied to the odd and even mirrors of each actuator of a single column modulator, creating a two dimensional voltage matrix, with optical power measurements conducted for the interferometric-phase and intensity-only cases. A simulation was created to compare the result with theory. Fig. 15 shows the simulation and measurement for detected power in these measurements. The  $x$ -axis is the odd mirror displacement and the  $y$ -axis is even mirror displacement.  $Z$ -axis represents the normalized power that was detected. As we can see, the measured results remarkably match the simulations. A maximum power attenuation of -26 dB was measured, and full  $2\pi$  phase modulation was achieved. Phase variation can

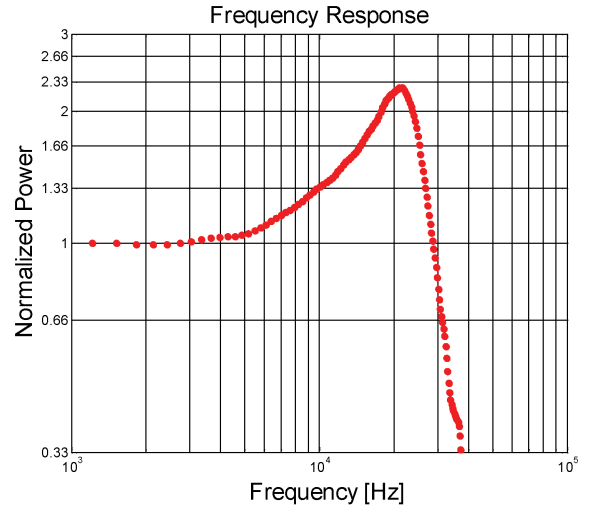


Fig. 16. Mechanical frequency response of a single actuator. Red marks are experimental data and blue curve is the theoretical fit.

be barely seen when the SLM in high attenuation configuration since the light reflected from the SLM is very weak compared to the light reflected from the reference mirror. But when the SLM operates in low attenuation configuration, phase variation can be seen very well.

The resonant frequency of the mechanical structure was measured (Fig. 16) actuating only the even pixels with a square wave and detecting the reflected power. We measured the time response of the light intensity with a sufficiently fast photodetector and extracted the frequency response from the step response measurements. The resonant frequency we observed is 24.2 kHz and  $Q$ -factor was calculated to be  $Q=1.4$ . In comparison, the mechanical simulation showed a resonant frequency of 28.2 kHz which again is indicative of weaker springs in our actuator than designed.

## V. CONCLUSION

We had realized a MEMS SLM able to modulate spectral phase and amplitude, capable of prescribing any amplitude and phase combination to dispersed light at the optical communication band. The device was optimal in the sense that two actuators/voltages alone were required to be driven per spectral element, even though many pixels were simultaneously driven by mechanical coupling with underlying structures. The dimension of each micromirror in the array was  $35 \mu\text{m} \times 35 \mu\text{m}$ , with a fill factor of 94.35%, and our array consisted of 12 columns along the dispersion axis and 33 mirrors in the orthogonal direction. Those values could be scaled up to any desired values, depending on optical design requirements or die size limitations. This MEMS modulator offered a large working range (mirror sag up to  $1.2 \mu\text{m}$ ), sufficient for modulating light from the visible range (400 nm) to mid-IR ( $\sim 2000$  nm). Our interferometric experiment confirmed that each spectral component could be encoded with any phase from 0 to  $2\pi$  and amplitude could be controlled continuously. This MEMS modulator could be useful in many spectral processing systems, from adaptive filters to pulse shaping applications.

## ACKNOWLEDGMENT

The authors acknowledge Prof. Y. Nemirovsky for the use of the Wyko interferometric microscope and the staff of the Hebrew University NanoFabrication Unit for their assistance in mirror metalization.

## REFERENCES

- [1] D. Sadot and E. Boimovich, "Tunable optical filters for dense WDM," *IEEE Commun. Mag.*, vol. 36, no. 12, pp. 50–55, Dec. 1998.
- [2] J. E. Ford and J. A. Walker, "Dynamic spectral power equalization using opto-mechanics," *IEEE Photon. Technol. Lett.*, vol. 10, no. 10, pp. 1440–1442, Oct. 1998.
- [3] R. Ryf, Y. Su, L. Moller, S. Chandrasekhar, L. Xiang, D. T. Neilson, and C. R. Giles, "Wavelength blocking filter with flexible data rates and channel spacing," *J. Lightw. Technol.*, vol. 23, no. 1, pp. 54–61, Jan. 2005.
- [4] J. E. Ford, V. A. Aksyuk, D. J. Bishop, and J. A. Walker, "Wavelength add-drop switching using tilting micromirrors," *J. Lightw. Technol.*, vol. 17, no. 5, pp. 904–911, May 1999.
- [5] D. M. Marom, D. T. Neilson, D. S. Greywall, P. Chien-Shing, N. R. Basavanahally, V. A. Aksyuk, D. O. Lopez, F. Pardo, M. E. Simon, Y. Low, P. Kolodner, and C. A. Bolle, "Wavelength-selective  $1 \times K$  switches using free-space optics and MEMS micromirrors: Theory, design, and implementation," *J. Lightw. Technol.*, vol. 23, no. 4, pp. 1620–1630, Apr. 2005.
- [6] D. T. Fuchs, C. R. Doerr, V. A. Aksyuk, M. E. Simon, L. W. Stulz, S. Chandrasekhar, L. L. Buhl, M. Cappuzzo, L. Gomez, A. Wong-Foy, E. Laskowski, E. Chen, and R. Pafchek, "A hybrid MEMS-waveguide wavelength selective crossconnect," *IEEE Photon. Technol. Lett.*, vol. 16, no. 1, pp. 99–101, Jan. 2004.
- [7] M. M. Wefers and K. A. Nelson, "Programmable phase and amplitude femtosecond pulse shaping," *Opt. Lett.*, vol. 18, pp. 2032–2034, 1993.
- [8] M. M. Wefers and K. A. Nelson, "Generation of high-fidelity programmable ultrafast optical waveforms," *Opt. Lett.*, vol. 20, pp. 1047–1049, 1995.
- [9] S. M. Weber, L. Bonacina, W. Noell, D. Kiselev, J. Extermann, F. Jutz, S. Lani, O. Nenadl, J.-P. Wolf, and N. F. de Rooij, "Design, simulation, fabrication, packaging, and characterization of a MEMS-based mirror array for femtosecond pulse-shaping in phase and amplitude," *Rev. Sci. Instrum.*, vol. 82, p. 075106, 2011.
- [10] S.-W. Chung and Y.-K. Kim, "Design and fabrication of  $10 \times 10$  microspatial light modulator array for phase and amplitude modulation," *Sens. Actuators*, vol. 78, pp. 63–70, 1999.
- [11] D. Sinefeld and D. M. Marom, "Colorless photonic spectral processor using hybrid guided-wave/free-space optics arrangement and LCoS modulator," in *Proc. Conf. Optical Fiber Communication (OFC)*, 2009, pp. 1–3.
- [12] J. Kondis, B. A. Scott, A. Ranalli, and R. Lindquist, "Liquid crystals in bulk optics-based DWDM optical switches and spectral equalizers," in *Proc. 14th Annu. Meeting IEEE Lasers Electro-Optics Soc.*, vol. 1, 2001, pp. 292–293.
- [13] E. Ranalli and B. Scott, "Wavelength Selective Switch," U.S. Patent 6 285 500, September 4, 2001.
- [14] T. Zhou, D. O. Lopez, M. E. Simon, F. Pardo, V. A. Aksyuk, and D. T. Neilson, "MEMS-based 14 GHz resolution dynamic optical filter," *Electron. Lett.*, vol. 39, no. 24, pp. 1744–1746, Nov. 2003.
- [15] M. Knapczyk, A. Krishnan, L. Grave de Peralta, A. A. Bernussi, and H. Temkin, "Reconfigurable optical filter based on digital mirror arrays," *IEEE Photon. Technol. Lett.*, vol. 17, no. 8, pp. 1743–1745, Aug. 2005.
- [16] G. Wilson, C. J. Chen, P. Gooding, and J. E. Ford, "Spectral filter with independently variable center wavelength and bandwidth," *IEEE Photon. Technol. Lett.*, vol. 18, no. 15, pp. 1660–1662, Aug. 2006.
- [17] K. Yu and N. Park, "Characterization of MEMS optical bandpass filters with narrow transition bands," in *Proc. SPIE—Optical Transmission Switching Subsystems III*, Shanghai, China, 2005, vol. 6021, pp. 2R1–2R8.
- [18] J. E. Ford, V. A. Aksyuk, D. J. Bishop, and J. A. Walker, "Wavelength add-drop switching using tilting micromirrors," *J. Lightw. Technol.*, vol. 17, no. 5, pp. 904–911, May 1999.
- [19] J. C. Vaughan, T. Hornung, T. Feurer, and K. A. Nelson, "Diffraction-based femtosecond pulse shaping with a two-dimensional spatial light modulator," *Opt. Lett.*, vol. 30, pp. 323–325, 2005.
- [20] E. Frumker and Y. Silberberg, "Phase and amplitude pulse shaping with two-dimensional phase-only spatial light modulators," *J. Opt. Soc. Amer. B*, vol. 24, pp. 2940–2947, 2007.
- [21] D. López, V. Aksyuk, G. Watson, M. E. Simon, W. Mansfield, F. Klemens, R. Cirelli, E. Ferry, A. Papazian, F. Pardo, C. Bolle, N. Basavanahally, J. Bower, J. Miner, T. Sorsch, and D. Tennant, "Two dimensional MEMS piston array for DUV optical pattern generation," in *Proc. Optical MEMS Their Applications Conf.*, vol. 1, 2006, pp. 148–149.
- [22] O. Solgaard, F. S. A. Sandejas, and D. M. Bloom, "Deformable grating optical modulator," *Opt. Lett.*, vol. 17, pp. 688–670, 1992.
- [23] [Online]. Available: <http://www.mems.sandia.gov/tech-info/summit-v.html>

**Jonathan Dunayevsky** received the B.Sc. degree in physics in 2007 and the M.Sc. degree in applied physics in 2011, both from The Hebrew University of Jerusalem, Israel. He is now with Oclaro Corporation, where he works on development of multiport optical switching solutions and MEMS devices for optical communications.

**Dan M. Marom** (M'00–SM'07) received the B.Sc. degree in mechanical engineering and the M.Sc. degree in electrical engineering, both from Tel-Aviv University, Tel-Aviv, Israel, in 1989 and 1995, respectively, and was awarded a Ph.D. in electrical engineering from the University of California, San Diego (UCSD), in 2000.

In his doctoral dissertation he investigated femtosecond-rate optical signal processing with applications in ultrafast communications. From 1996 through 2000, he was a Fannie and John Hertz Foundation Graduate Fellow at UCSD. From 2000 until 2005, he was a member of the Technical Staff at the Advanced Photonics Research Department at Bell Laboratories, Lucent Technologies, where he worked on novel MEMS based switching solutions for optical communications. Since 2005, he has been with the Applied Physics Department, The Hebrew University of Jerusalem, where he is pursuing his research interests in creating photonic devices for switching and manipulating optical signals, using light modulating devices, nonlinear optics, and compound materials. Dr. Marom is also a member of the Optical Society of America. He was a Peter Brojde Scholar in 2006–2007, and has served as an Associate Editor for *Photonics Technology Letters* since 2007.